Toward an ultracold mixture of Er and K

Gavin Lamb
Wolfson College
University of Oxford

A report submitted for transfer of status to
Doctor of Philosophy
26/08/2022

Abstract

In this report I detail the continued construction of a dual species dipolar quantum gas experiment of erbium and potassium. Currently an Er Bose Einstein condensate (BEC) has been achieved and work is ongoing in the construction of the K setup to allow for the inclusion of a second species. After completion, this dual species BEC will be transported to a second chamber known as the science cell. My work primarily focuses on the design and construction of the optics and coils required to trap and manipulate the atoms within the science cell. The trap will have a quasi 2D "pancake" shape which will allow for the investigation of the roton minimum which is thought to be responsible for the formation of quantum droplets and supersolids. Additional work has also been completed in calibration of Feshbach coils using RF spectroscopy. The group have completed a significant optimisation and stabilisation of the machine and have begun experimentation, on 3 body loss and quantum droplet experiments. Once complete, the dual species experiment will be an ideal platform for studies of impurity physics relevant for the study of condensed matter.

Declaration

I declare that this work has been composed solely by myself and that it has not been submitted, in whole or in part, in any previous application for a degree. Except where stated otherwise by reference or acknowledgment, the work presented is entirely my own.

Contents

1 Introduction

A Bose Einstein Condensate (BEC) is a state of matter which occurs when a dilute gas of bosonic atoms are taken to temperatures just above absolute zero. In these conditions the atoms can reach quantum degeneracy and macroscopically occupy the ground state. This phase transition was first predicted by Bose and Einstein in 1925. However, it was not until 1995 that first experimental observation of a BEC was made by Cornell and Wieman [1], using in a Rb gas (see figure 1), and afterwards, in Na [2] by Ketterle; all three later shared the Nobel Prize [3]. Currently 13 elements have been cooled to quantum degeneracy including Er [4] and K [5] which are of specific interest to our group.

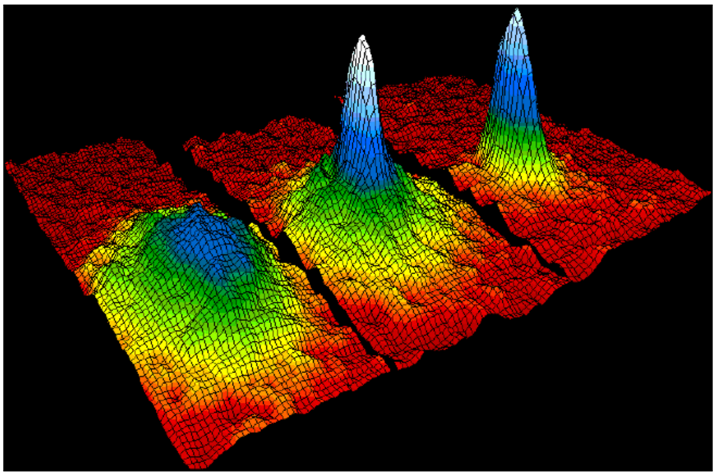

Figure 1: The first observation of a BEC in Rb in 1995 [6]. False color 3D plots after a time of flight measurement in 3 atomic clouds. Both the height and colour indicate atomic density. The left most plot shows a thermal cloud just before condensation. The middle plot is taken just after the formation of the BEC, containing a mixture of BEC and thermal cloud. Finally the right most plot shows the BEC after further evaporation leaving a pure BEC with no thermal cloud. The thermal cloud and BEC are characterised by their distributions. The non condensate fraction is an isotropic enhanced Bose distribution. Whereas the BEC fraction is anisotropic, due to the trapping geometry, and parabolic.

Some of the atoms that have been cooled to quantum degeneracy also exhibit a magnetic dipole-dipole interaction (DDI), for example Cr [7], Er [4] and Dy [8], due to their large magnetic moment. Unlike the standard contact interaction, the DDI is long range and anisotropic. It therefore provides a platform for unusual behaviour associated with the the theoretically predicted roton excitation spectrum [9] which exhibits at finite momentum (see figure 2) [10]. Tuning the depth of this roton minimum can lead to the formation of quantum droplets [11, 12, 13, 14] and with specific parameters to a supersolid phase [15, 16, 17].
Another key area of interest for the group is in dual species BEC physics [18]. This is motivated by the analogy to condensed matter systems in which one species can play the role of an impurity and the other the interacting background. The resulting physics can then be separated into 2 categories depending on if the background atoms are fermionic or bosonic. In the fermionic case, the system corresponds to a magnetic impurity in a sea of electrons known as the Kondo problem [19]. If the background is bosonic, the system instead corresponds to an electron in a background of phonons. It is thought that this system could help explain high temperature superconductivity [20] or colossal magneto resistance [21]. These phenomena are connected by the presence of a polaron, a quasi particle which represents an impurity with its interacting background [22].
In our experiment, we plan to study these physical phenomena via the use of a dual species Er+K BEC experiment. This transfer deals with elements of its construction as well as significant scientific goals achieved in the last year.

2 Laser Cooling of Er

Laser cooling techniques are a key ingredient needed for reaching the temperatures required for BEC [23, 24, 25]. In our experiment, we first slow a beam of atoms using a Zeeman slower before trapping and further laser cooling them in a Magneto-optical trap (MOT). Both of these techniques rely on the scattering force which results from a photon's momentum being absorbed by an atom so that it receives a momentum kick. If this momentum kick opposes the motion of the atom it results in slowing and thus often cooling.

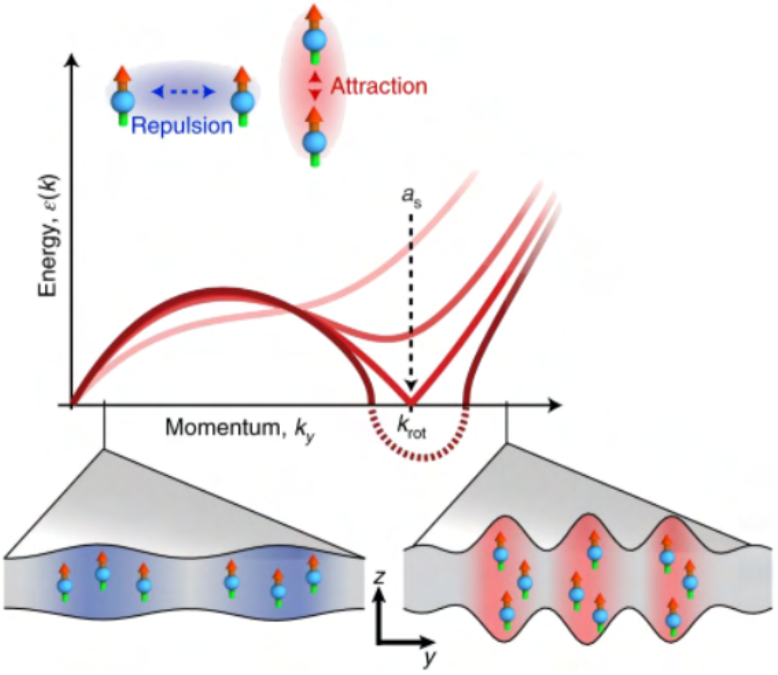

Figure 2: Energy dispersion relation of a 2D dipolar quantum gas containing a roton minimum. The repulsive and attractive interactions of the dipole are shown as well as how excitations at certain k can lead to a displacement of dipoles from the transverse plane to the vertical direction at which point there interaction becomes attractive leading to the roton minimum. [26]

2.1 Zeeman Slower

In a Zeeman slower, a laser beam is set up in opposition to a beam of atoms (typically coming from an oven) and so the scattering force leads to slowing of the atomic beam.
As the velocity of the atoms are reduced the incoming photons are Doppler shifted by a different amount and so the laser light shifts off resonance of the atomic transition. This is compensated for using the Zeeman effect: a tapered solenoid is set up along the atomic beam such that a position dependent magnetic field is produced (see figure 3) which can be used to shift the energy levels of the atoms using the Zeeman effect in such a way that it cancels the changing Doppler shift.
In order to capture high velocity atoms a broad linewidth transition is required (We use the Er 401 nm transition which has a linewidth of 30 MHz).

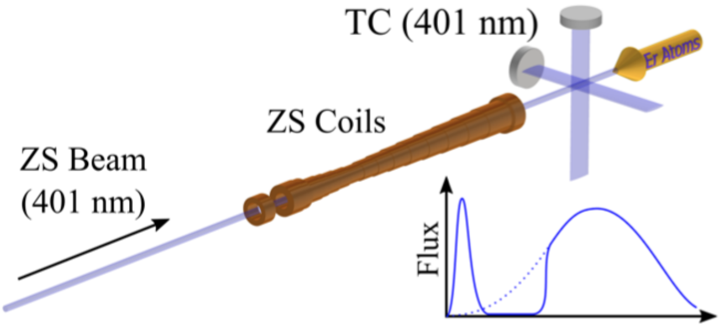

Figure 3: Graphic showing the solenoid coil along the beam path of the Zeeman slower [28]. Also shown is the transverse cooling (TC) beams used to reduced velocity in the transverse plane of the beam direction. Inset graph shows the velocity distribution with (blue) and without (dotted) the effect of the Zeeman slower.

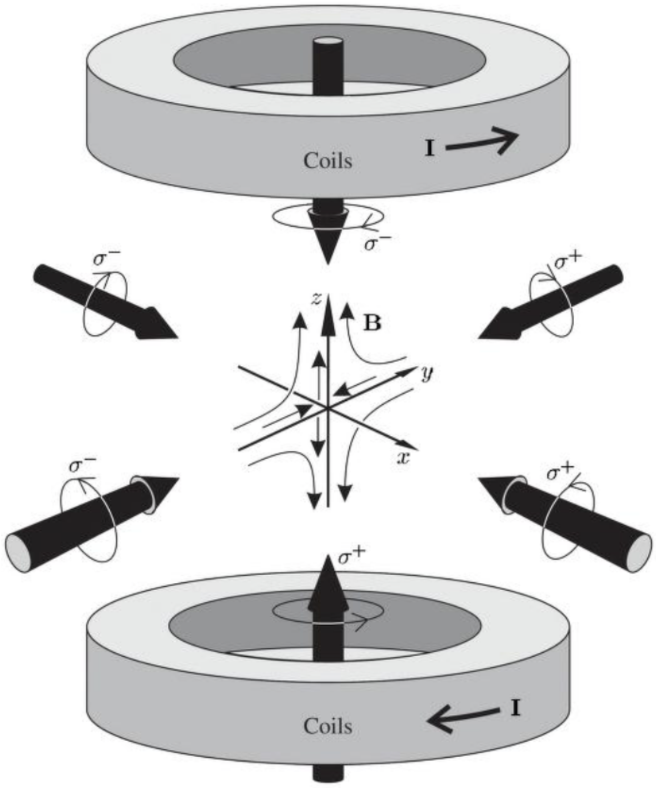

Figure 4: The Magneto Optical Trap which is created by a combination of a quadrupole field generated by the pair of coils shown, as well as the 6 counter propagating beams along 3 orthogonal directions. The counter propagating beams have opposite polarisation such that when combined with atomic selection rules the atoms only absorb oncoming photons and are therefore slowed [27].

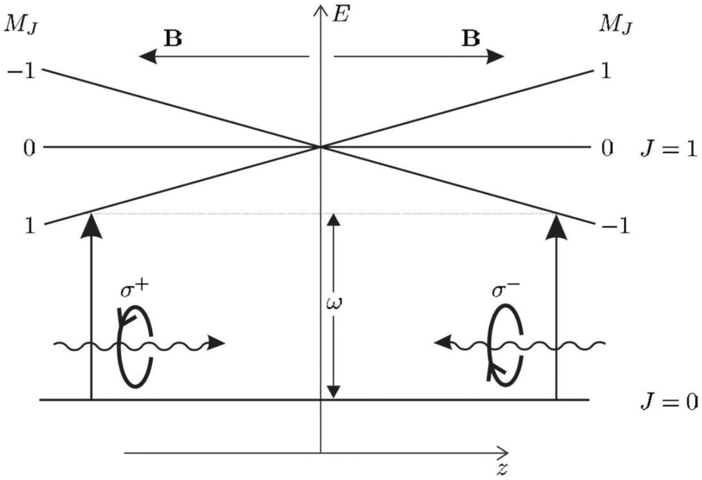

Figure 5: Energy level diagram created by the MOT. The counter propagating beams have opposite polarisations such that they only excited atoms opposing their direction due to atomic transition selection rules. This leads to a position dependent trap in which atoms can be cooled [27].

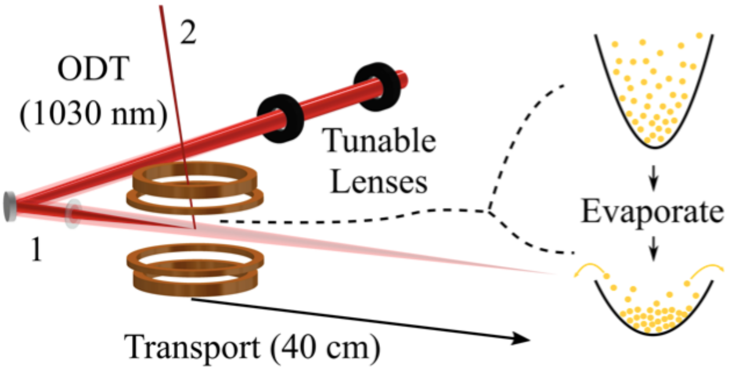

Figure 6: The Optical Dipole Trap set up [28]. Shown are the two cross beams along with the tunable lenses which will be used to transport the BEC to the science cell. Energy potentials show the effect of evaporation as high energy atoms are lost such that the average temperature of those that remain decreases.

2.2 Magneto-Optical Trap

To perform the next stage of cooling, a MOT is used which, in addition to cooling the atoms, will generate a spatial trap [27]. In this case, light is now directed at the atoms in all 6 orthogonal directions as seen in figure 5. If the atoms were to absorb photons in all directions there would be no cooling effect but using red-detuned light means that photons are only absorbed if they interact with a counter propagating atom.

Additionally a quadrupole magnetic field is applied which splits the degeneracy of the excited state. This also produces a position dependent Zeeman shift similar to the Zeeman slower. This, together with carefully choosing the polarisation of the light results in trapping as well as cooling (see figure 4)

Our MOT uses a narrower linewidth transition (190 kHz) than the Zeeman slower which allows for a lower cooling limit, that is set by the so-called Doppler limit which is proportional to linewidth. This does result in a smaller capture velocity but as the Zeeman slower has already reduced the velocity of the incoming atoms this is now acceptable.

3 Creating a Bose Einstein Condensate of Er

3.1 ODT and Evaporation

It is not usally possible via the use of laser cooling to achieve the temperatures required for BEC due to the recoil limit. Instead another cooling method known as evaporative cooling is used. In our experiment this works via the use of an optical dipole trap (ODT) [28] however it is also possible to evaporate in a magnetic trap [1]. The ODT is generated by polarising atoms via the application of a high intensity laser beam. These polarised atoms are then attracted to higher intensity regions of a red detuned beam. If a small beam waist is set up, the atoms can be trapped within the beam waist. This can also be assisted by the addition of a second cross beam which increases confinement further. Our experimental setup for this is shown in figure 6.

By slowly lowering the intensity of the laser used for trapping and therefore lowering effective depth of the trap, the atoms with the highest energy will escape. After allowing the atoms to re-thermalise the average energy of the atoms (and therefore the temperature) is reduced at the expense of reduced atom number. It is this process which allows us to reach the temperatures required for BEC.

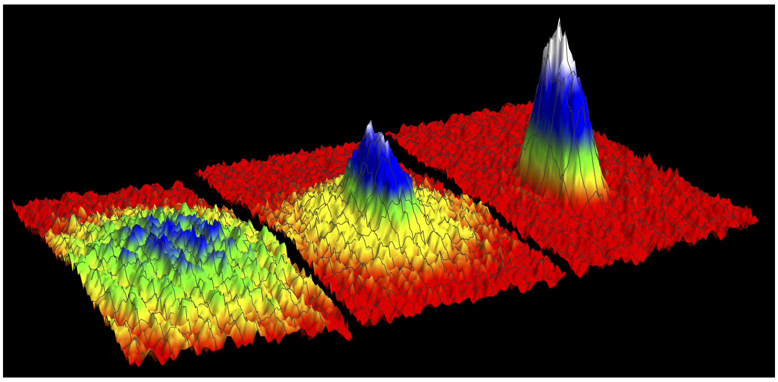

Figure 7: Data from our Er experiment shown in the same format at figure 1. The left shows a thermal cloud just before condensation. The middle graph is just after condensation and so contains both a thermal cloud and BEC component. Finally, the right graph is after further evaporation and therefore is a close to a pure BEC. Quantitative fits of these 3 clouds are shown in figure 30,31 and 32

3.2 Erbium BEC Milestone

In December of 2021, the group passed the significant experimental goal of producing a Er BEC. Figure 7 shows absorption images of the evaporation stages toward a BEC, in same format as figure 1, produced by our experiment. The bimodal distribution can clearly be seen which is indicative of the thermal cloud and BEC mixture. However, for a more quantitative measurement a program was developed to fit the data. This is detailed in section 6.3.2 along with the fits for the 3 clouds as shown in figure 7.

3.3 Feshbach Coil Calibration using RF spectroscopy

3.3.1 Feshbach Resonance

An important parameter for the production and use of erbium BECs is the scattering length. The strength of the contact interactions between atoms can be control via the phenomenon of a Feshbach resonance [29]. The unusual phenomenon occurs when the energy of a bound state is equal to the kinetic energy of 2 approaching particles. The two particles can form a molecule with a short lifetime which leads to a modification of the scattering length. An applied DC magnetic field can shift the relative energies involved leading to this equality in energy and therefore the application of such a field can tune the scattering length of an atomic gas. An example of how the Feshbach resonances effect the scattering length as a function of field is shown in figure 8

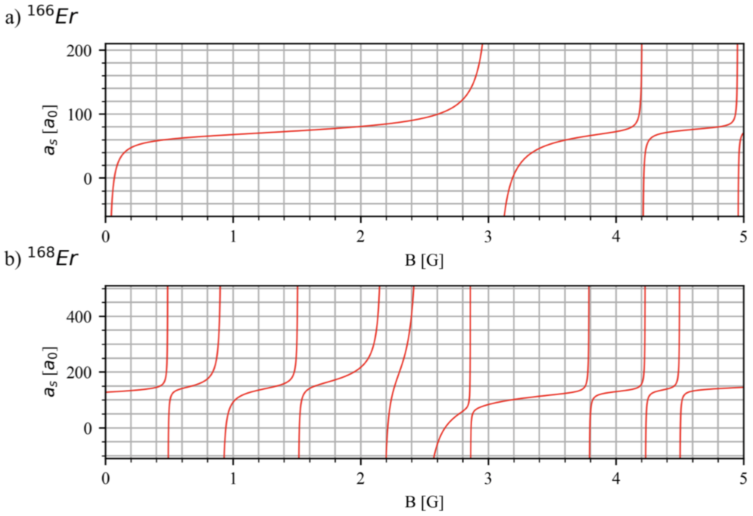

Figure 8: Feshbach resonances in the 0-5 G range in both 166Er and 168Er. The resonances allows for the control of the scattering length of an atomic gas via the application of a DC magnetic field. Data from [30, 31].

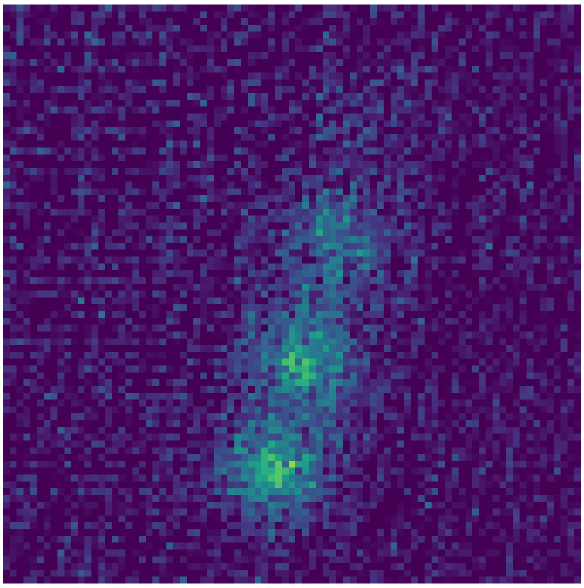

Figure 9: A BEC split into 3 visible sub clouds after a Stern Gerlach experiment. The RF coil was used to pump the BEC between its M_j states which have been split by another DC applied field. When the applied field (generating a Zeeman splitting) is resonant with the RF frequency, splitting is seen after being dropped through a gradient field constituting a Stern Gerlach experiment. This means the exact DC applied field can be calculated via the frequency at which the splitting is seen.

3.3.2 RF spectroscopy calibration

In our experiment the DC field required to manipulate the scattering length of the atoms is control by a set of 'Feshbach coils' which are in the Helmholtz configuration in the vertical direction. To calibrate the magnetic field at the centre of the MOT chamber we us radio frequency (RF) spectroscopy of the ground-state Zeeman splitting in erbium. The ground state or erbium is a $J = 6$ state with a manifold of 13 M_J states ($M_J =$ -6, -5 ...5, 6) which are linearly split in the presence of a magnetic field B by the Zeemen effect. Applying RF radiation at a frequency f equal to this splitting transfers atoms between the different M_J states; this condition is given by,

$$\Delta f = \frac{\mu_B g_g B}{2\pi\hbar} = 1.6288\frac{MHz}{G} \times B \tag{1}$$

where g_g is the ground state Lande factor and $_B$ is the Bohr magneton. We generate the RF field using a 40 turn coil placed in the top view port of the MOT chamber and drive it with an (amplified) sinusoidal voltage from a signal generator. The design and testing of the RF coils are describe in section 6.2. The erbium atoms trapped in our ODT are spin-polarized in the $M_J = 6$ state as a result of optical pumping in the MOT due to gravity. We can thus calibrate the magnetic field by applying RF radiation and finding the resonant f [equation1] that leads to the population of higher M_J states. To measure the different M_J state populations we spatially separate them using a magnetic field gradient in a Stern-Gerlach like experiment and observe them using absorption imaging. An example of an image of multiply populated, spatially separated, M_J states is shown in Figure 9. Such images allow us to accurately determine B using equation 1 for a given applied Feshbach coil current I_Fesh; the resulting calibration curve is shown in figure 10. At low current the relationship to magnetic field is non linear due to a non negligible contribution background magnetic field (e.g. due to the earths magnetic field) which has both vertical z and horizontal x components. Thus, the data is fitted to,

$$B = \sqrt{(CI_{Fesh} + B_{bkd,z})^2 + B_{bkd,x}^2} \tag{2}$$

where $B_{bkd,x(z)}$ are the horizontal (vertical) components the background magnetic and $C = 1.992$ is the current to magnetic field ratio of the Feshbach coils.

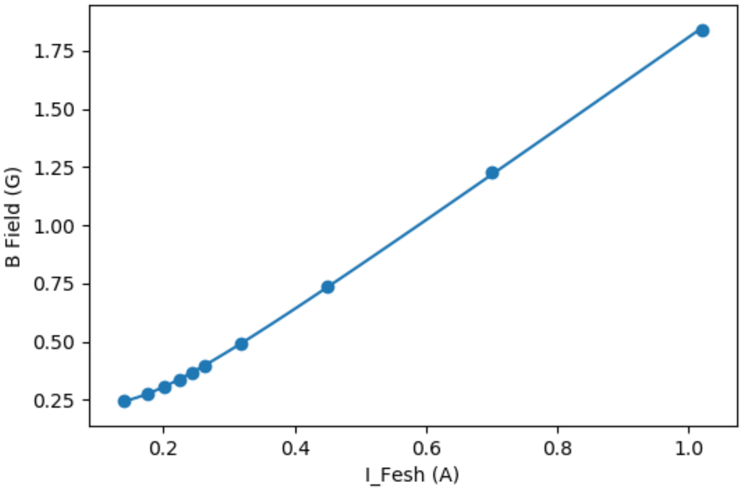

Figure 10: The field at which cloud splitting during a Stern Gerlach experiment is observed against the Feshbach current used to generate the magnetic field. At low current and therefore field, the Earths magnetic field has a non negligible effect as seen by the curve in the data below 0.3 A. At high current the relationship is linear and the ratio between field and current found to be 1.992 G/A.

4 Science Cell

After a BEC is formed in the MOT chamber, it can be used for various experiments to probe physics as discussed in section 5. However, the various optical and magnetic components which have been used to generate the Zeeman slower, MOT and ODT heavily restrict optical access to the centre of the chamber in which the BEC is held. This optical access is vital for future experiments. To regain it the BEC is moved to a second chamber known as the science cell (see figure 11).

As shown in figure 6, the ODT set up contains 2 tuneable lenses which can be used to move the focal position which sets the trap location. As there are 2 lenses this can be achieve while maintaining a constant beam waist. The focus position of ODT1 can be adjusted so that it resides within the centre of the science cell. Currently testing is being undertaken to optimise the correct speed and shape of the ramp which will generate this transport. Once in the science cell an optical trap will confine the BEC. The aim is for this trap to be a quasi 2D "pancake" shaped trap, with a $\sim$30 μm radius, as shown in figure 12. The formation of this trap is discussed in section 4.2. This confinement will allow for interesting observations as discussed in section 5. Along with this trap a set of magnetic field coils will be used to manipulate the dipoles and explore Feshbach resonances as discussed in section 4.1.

4.1 Coils

One major aspect of the experimental setup of the science cell is the magnetic field coils which can be categorised into 2 sets, large and fast. Firstly, the large set of coils will allow the high field Feshbach resonances of 41 K and 39 K to be reached, shown in table 1 and 2.

We aim to reach a magnetic field up to at least 162.8 G, corresponding to the resonance in 39K. The high field will also allow for exploration of the Feshbach resonances in the Er+K mixture which are currently experimentally unknown.

A second set of fast coils can be used to produce an AC field which will rotate the dipoles around their axis. If this rotation is fast then the time averaged effect is to see a smaller magnitude dipole. This allows the dipole dipole interaction to be tuned in the experiment as shown in figure 13.

State	Field (G)	Width (G)
1,-1	51.35	-0.3
1,1	409	0.03
1,1	660	0.2

Table 1: Feshbach resonances in 41K. Data taken from [32],[33].

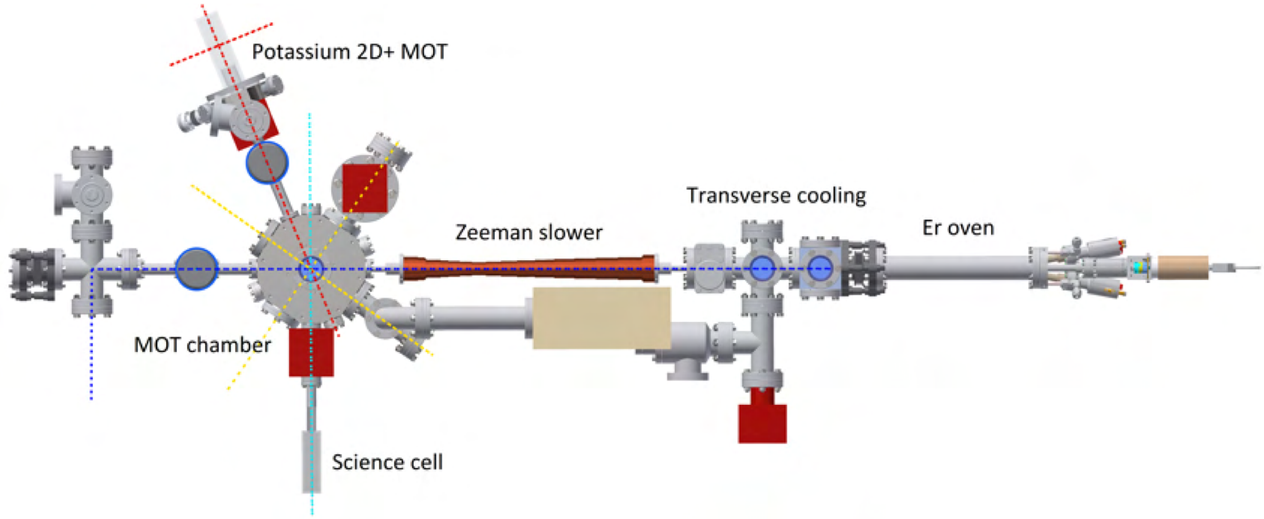

Figure 11: 2D model of the vacuum system [28]. Atoms begin in the oven and travel to the left first being transversely cooled before being slowed from several hundred m/s to a few m/s by the Zeeman slower (shown in blue). They are then trapped in the MOT chamber which is generated by a combination of coils (not pictured) as well as light in 6 orthogonal directions (4 in plane beams shown in yellow). They can then be loaded into a cross trap ODT beam (ODT1 in plane beam shown in cyan) used for evaporation down to a BEC. The K 2D+ MOT is still under construction but is also shown and will be used to generate the dual species BEC. Finally the science cell is shown in the beam direction of ODT1. After generating a BEC atoms can be transported here via the use of the two tune-able lenses in the ODT setup to move the trap location.

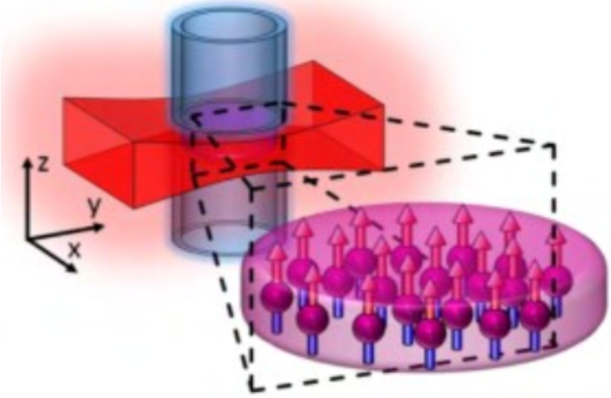

Figure 12: The quasi 2D “pancake” trap. The red sheet beam in the transverse plane is attractive and the blue cylindrical beam in the vertical direction is repulsive. Together these form the “pancake” shape trap shown in purple which contains a set of dipoles that can be manipulated by the application of magnetic fields.

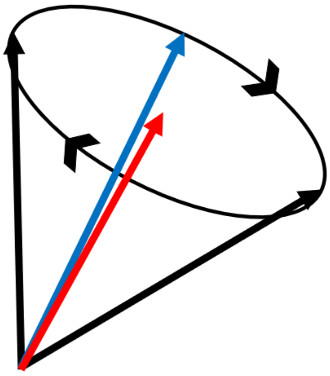

Figure 13: Dipole rotation to reduce dipole magnitude when time averaged. If the dipole represented by the blue arrow is rotated by fast AC fields such that it moves through the path in black (2 positions along this path represented by black arrows) then when time averaged the effective dipole will have a smaller magnitude as represented by the red arrow. This allows for the DDI strength to be tuned for experimental purposes.

State	Field (G)	Width (G)
1,1	25.91	-
-1,-1	33.5820	36.6
0,0	58.97	-
0,0	65.57	-
-1,-1	162.36	25.9
1,1	402.74	52.2
1,0	472.33	69.6
1,0	491.17	4.78
-1,-1	561.14	56.7
1,1	752.3	-

Table 2: Feshbach resonances in 39K. “-” indicates that it has not been experimentally determined. Data from [34].

4.1.1 Initial Work

A program was developed to allow for magnetic field coil designs to be evaluated. The program calculated both maximum magnetic field produced at a range of dipole angles as well as the homogeneity of the field in the Cartesian directions. An initial coil design is shown in figure 14 (figure 33 and 34 in the Appendix show the fast and large coils individually for better clarity). However, there were multiple issues which required assessment. Figure 15 shows the maximum magnetic field achievable against dipole angle and figures 16 and 17 shows the homogeneity of the field in each direction at high and low field. The first issue is based on the lack of homogeneity of the magnetic field indicating that the coils are not in a Helmholtz configuration. The second concerns inductance, firstly the fast coils are made of 64 loops of wire and therefore have a high self-inductance as shown in table 4. There is also concern that the fast coils rectangular nature implies that they have long sections running parallel to each other and that therefore the mutual inductance between them may be significant. Both self and mutual inductance will inhibit the fast operation of these coils potentially reducing their effectiveness. It was therefore the aim to both increase the homogeneity of the fields as well as reduce both the self and mutual inductance of the fast coils.

4.1.2 Inductance Code

A program was written to calculate the mutual inductance between any two rectangular or circular coils, in free space, both at any rotation. This is achieved by a numerical integration using the Biot-Savart law, equation (3), to find the magnetic field generated by one loop at each point within the area of a second loop. From this, the magnetic flux through the second loop can be found via equation (4) and in turn the mutual inductance between the loops in equation (5). Figure 18 shows an example of points used to generate the $d\mathbf{l}$ vectors in equation (3) and $d\mathbf{a}$ vectors in equation (4). In this case a circular loop of radius 4 cm is used sitting in the transverse plane.

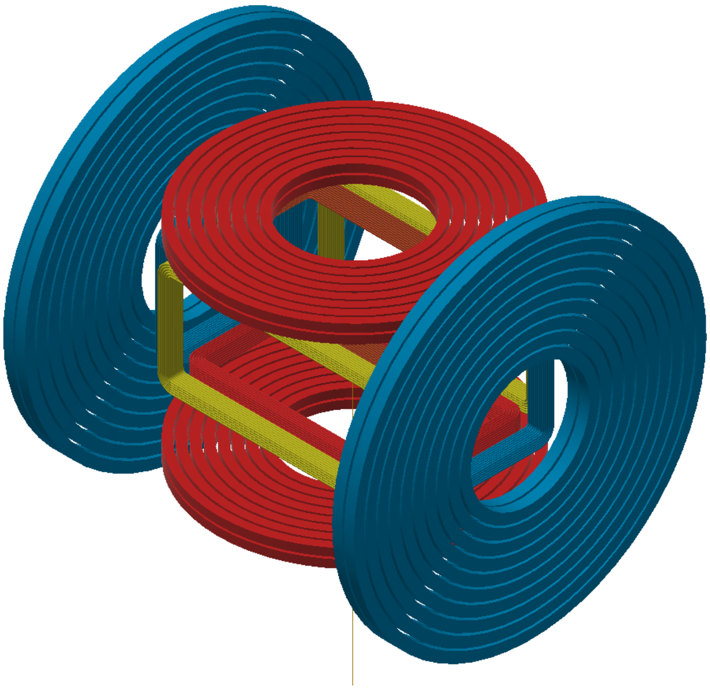

Figure 14: The original coil design. The X,Y and Z coils are shown in Yellow, Blue and Red respectively.

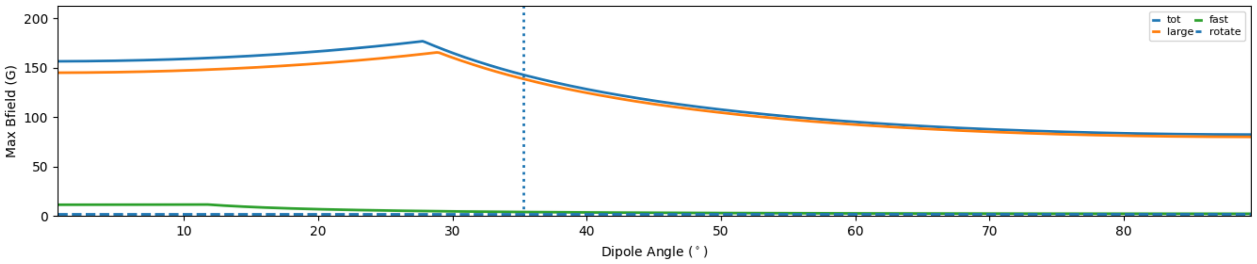

Figure 15: The simulated magnetic field achievable over a range of dipole angles using the initial design at 100 A. The dotted line indicates the magic angle of ≈ 35.26°. If the spins are aligned at this angle the DDI can be minimised

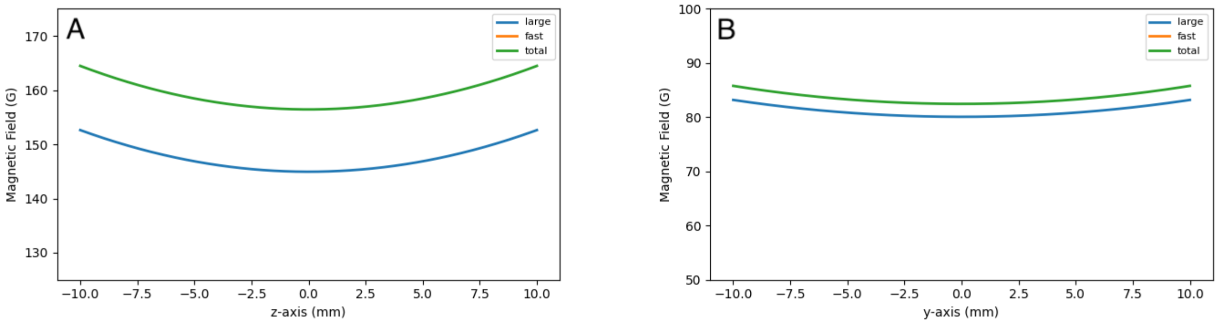

Figure 16: Plots showing the high field homogeneity of the large coils in the initial design. A and B are in the Z and Y direction respectively. The large curvature is indicative of non optimised coils.

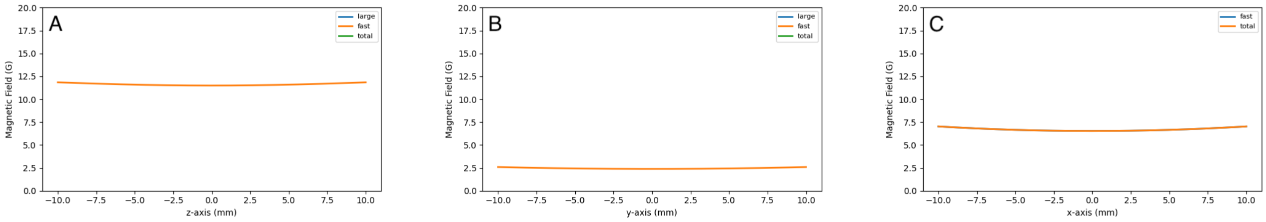

Figure 17: Plots showing the low field homogeneity of the fast coils in the initial design. A, B and C are in the Z, Y and X direction respectively. The curvature is indicative of non optimised coils.

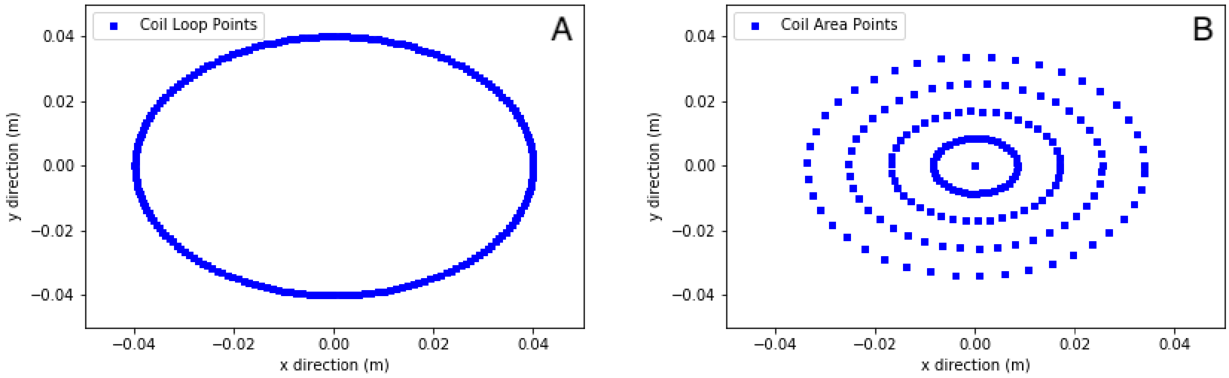

Figure 18: An example of the points used to generate the vectors required for the mutual inductance calculation. Shown is a 4 cm circular coil in the transverse plane. A shows the points along the loop of the coil used to generate the d**l** vectors for equation (3). B shows the points in the area of the coil used to generate the d**a** vectors for equation (4).

$$B_1 = \frac{\mu_0}{4\pi} I_1 \oint \frac{dl_1 \times \hat{r}}{r^2} \tag{3}$$

$$\phi_2 = \int B_1 \cdot da_2 \tag{4}$$

$$M_{21} = \frac{\phi_2}{I_1} \tag{5}$$

The code was verified against an approximation of mutual inductance which is detailed in section 6.1
The conclusion reached was that the largest mutual inductance, between the Z and X coils which share a long side length is 6.5 mH. For reference, the fast rectangular z coil has a self inductance of 1.05 mH. This means the mutual inductance is on the same order as the self inductance both of which are high. It was therefore chosen to change to a design to reduce both the direct overlap and the number of turns.

4.1.3 CAD design

The initial coils as shown in figure 14 were designed by Lucas Hofer, another DPhil student in the group. The issues with them have already been discussed in section 4.1.1. These issues largely came from designing a set of coils around a set of mounts. It was therefore decided that the coils would instead be designed first and a mounting solution for them found later. This may lead to a less elegant mounting however a better scientific set up which is the primary goal.
There were many factors to consider in the design of the large coils in order to obtain the aims as detailed in section 4.1, requiring a total field of over 162.8 G to be achieved over a range of dipole angles as well as retaining field homogeneity. In order to achieve this field the large coils will have to operate at over 100A. This means they will produce on the order of 250 W which has to be actively cooled. This is accomplished via the use of hollow copper tubing made by Luvata [35] which allows for pressurised water to flow through the coil. The cooling power of the coils can be calculated using equations (6),(7),(8).

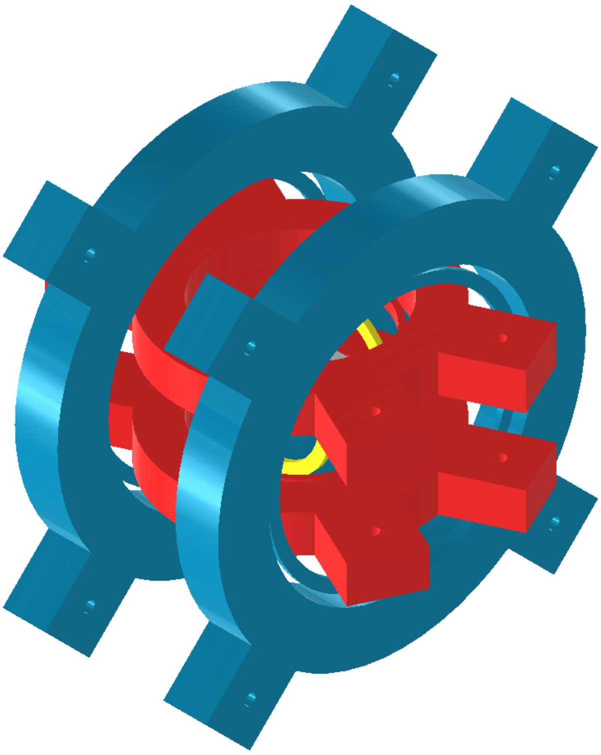

Figure 19: The updated and optimised coil design. The X,Y and Z coils are shown in Yellow, Blue and Red respectively. The large coils have additional tabs to allow for mounting. The fast coils will be mounted to these larger coils (Designs for this are still to be finalised).

$$P = Q\Delta T C_{water} \tag{6}$$

$$Q_{LFM} = \frac{\pi r \eta}{8\rho}\left(\frac{\rho r^3 \delta P}{\eta^2 l}\right) \tag{7}$$

$$Q_{TRM} \approx 38\frac{\pi r \eta}{8\rho}\left(\frac{\rho r^3 \delta P}{\eta^2 l}\right)^{4/7} if \left(\frac{\rho r^3 \delta P}{\eta^2 l}\right) \geq 5000 \tag{8}$$

Where ρ, η and C_{water} are the density, viscosity and heat capacity of the water. ΔT is the temperature raise of the water, r is the radius of the hollow section through which water flows, δP is the pressure differential over the coil and l is the length of the coil. Q is the flow rate and differs depending on the flow type of the water. In order to increase cooling power, the length of the coil can be split in 2 to create 2 separate cooling loops. After consultation with Oswald [36] (the company responsible for coiling the wire) it was decided that it would be possible to cool the designed coils with less than 5 bar using single cooling loops therefore reducing complexity and cost. The final design for the large coils can be seen in figure 19.

(Figure 35 and 36 in the Appendix show the fast and large coils individually for better clarity). They have been set up to be as Helmholtz-like as possible given the physical restrictions of the science cell as well as each other. The same program can be used to evaluate this coil design and the results are shown in figure 20, 21 and 22. To give a better quantitative measure of the improvement, a 2nd order polynomial fit was added to the code to allow for the coefficient of x^2 term to extracted and compared. A comparison between the new and old coils homogeneity can is shown in table 3. The new coils represent a significant improvement which will lead to improved field homogeneity in the future experiment. For further improvements, changes in position of the coils of less than 0.5mm are required. This is likely not possible experimentally, so the setup described was determined as the optimum.

The small fast coils have then been designed around the large coils and can be seen in figure 35. The design for these coils are not finalised. We will be able to develop and complete the design of the fast coils once we receive the final design for the large coils from Oswald. In the original design for the fast coils there were issues with both self and mutual inductance as discussed in section 4.1.1 and 4.1.2.

Direction, type	Old Setup Homogeneity (G/m^2)	New Setup Homogeneity (G/m^2)
Y, Large	2.841	0.008
Z, Large	6.581	0.012
X, Fast	0.477	0.072
Y, Fast	0.201	0.048
Z, Fast	0.344	0.074

Table 3: Comparison between the original and new optimised designed coils homogeneity. In the large coils 100 A is used and the fast coils are 1 and 8 A for the old and new setups.

Direction, type	Old Setup Self Inductance (mH)	New Setup Self Inductance (mH)
X, Fast	12.5	0.97
Y, Fast	31.0	0.66
Z, Fast	16.5	1.1

Table 4: Comparison between the original and new optimised designed coils self inductance.

To reduce self inductance only 8 turns carrying up to 8 A rather than 64 turns with 1 A are used. As self inductance is proportional to the turn number squared this provided a significant improvement. The improvements on self inductance are shown in table 4.

The mutual inductance between these coils has also been significantly reduced as they have less overlap as well as fewer turns. The largest mutual inductance is between the X and Z fast coils which is calculated to now be only 0.25 μH compared to the previous design of 6.5 mH.

We also aimed to keep these coils as Helmholtz like as possible, however, due to the large coils, the size and separation of these coils was more constrained so the final solution is not as fully optimised, the results from the program are shown in figure 22 and table 3. The Y coil can be better optimised by reducing the distance between the coils or increasing the radius, neither of which are possible. The X and Z coils can both individually be optimised to achieve improved results but in doing so it impedes the other so they have been optimised together.

4.2 Optical Design

The magnetic fields will be accompanied by an optical setup which will form the “pancake” shaped trap as shown in figure 12. This confinement will allow for interesting observations as discussed in section 5.

The “pancake” trap will be created by the overlap of 2 laser, an attractive red detuned sheet beam in the transverse plane and a repulsive cylindrical pseudo-Laguerre-Gauss (pLG) beam in the z direction. The pLG will be formed using a spatial light modulator (SLM). Two additional beams will be used for absorption imaging of Er and K. Finally, a digital micromirror device (DMD) will be setup to form a final beam which will probe the dispersion relation of the system. A preliminary setup for the optics is shown in figure 23.

The laser used for the sheet beam has been supplied by Azurlight [37] and is currently undergoing characterisation. The other lasers have already been acquired and therefore after finalising the design, work can begin on setting up this section of the experiment.

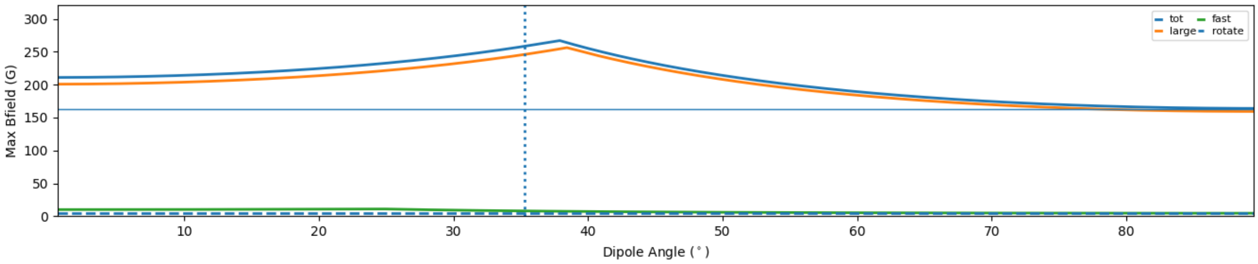

Figure 20: The simulated magnetic field achievable over a range of dipole angles using the optimised design at 100 A. The dotted line indicates the magic angle of ≈ 35.26°. The magnetic field is higher over all dipole angles and above the 162 G Feshbach resonance (indicated by the horizontal line) up to the magic angle.

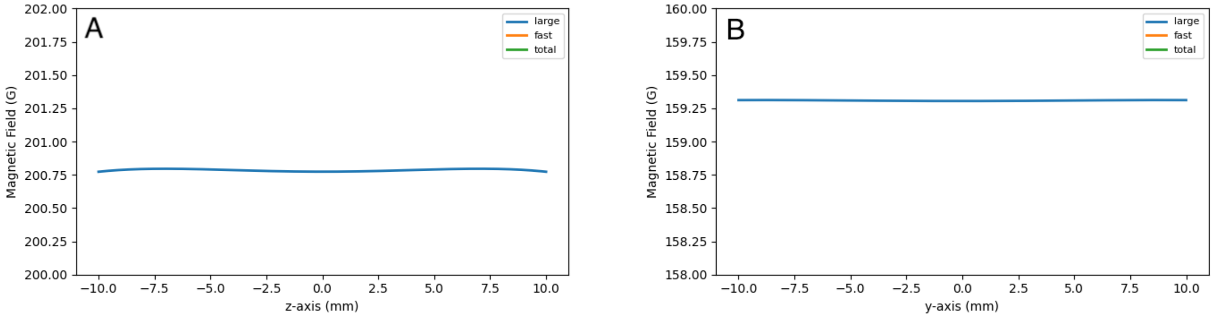

Figure 21: Plots showing the high field homogeneity of the large coils in the optimised design. Figure A and B are in the Z and Y direction respectively. The y range has been reduced to show any remaining curvature due to the large coils. This curvature has been reduced indicating a more optimised setup.

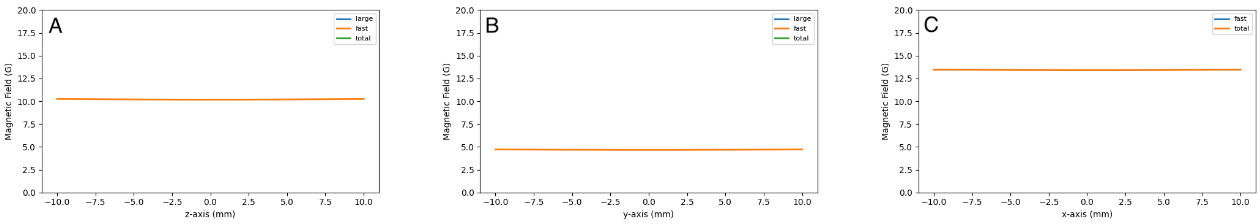

Figure 22: Plots showing the low field homogeneity of the fast coils in the optimised design.Figure A, B and C are in the Z, Y and X direction respectively. The curvature has been reduced indicating a more optimised setup.

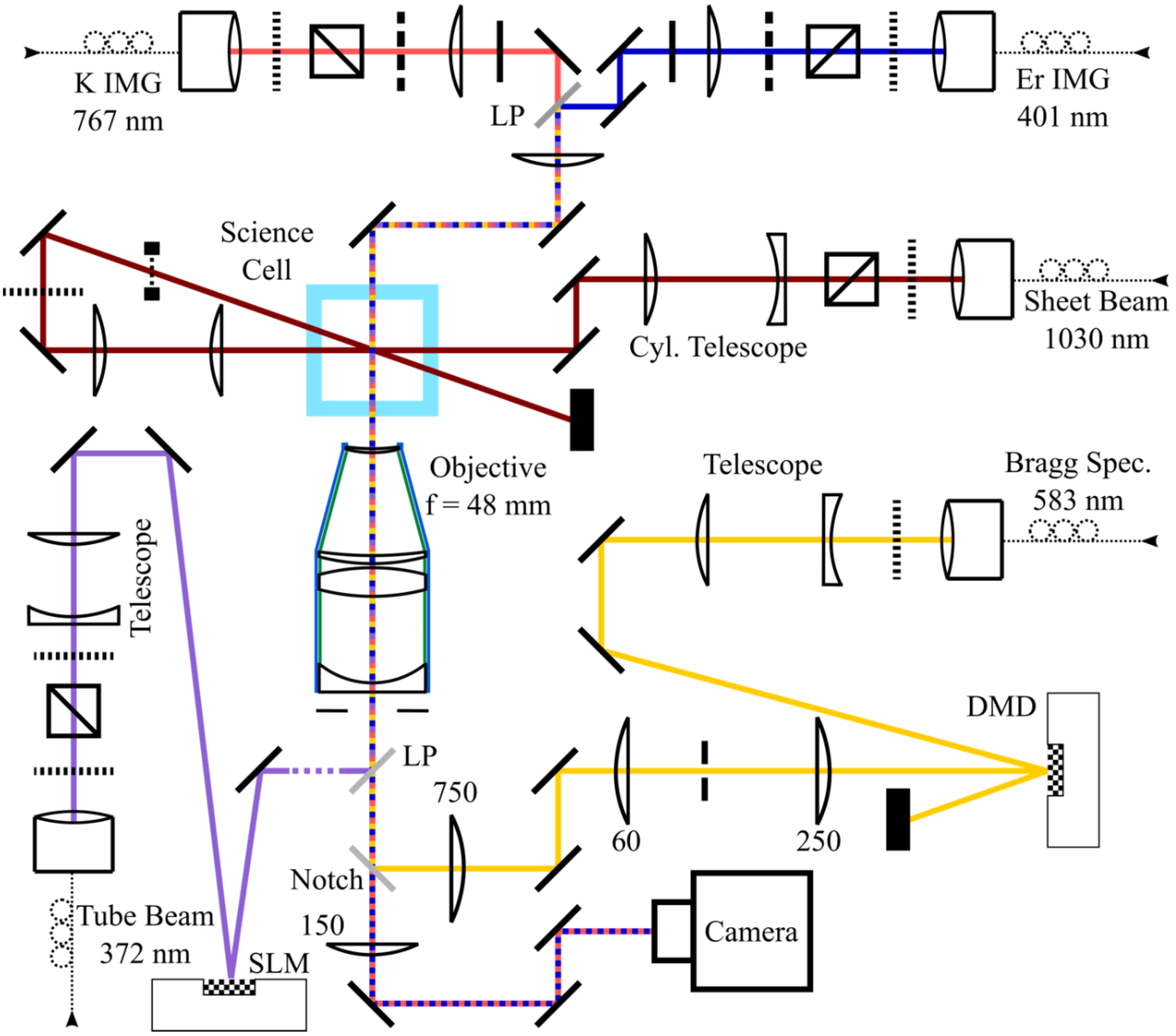

Figure 23: The preliminary design of all optical systems around the science cell [28]. 5 laser beams are shown which form the trap, probe and image the atoms. The 2 imaging beams (red and blue) are used for K and Er respectively. An attractive sheet beam (dark red) and repulsive cylindrical beam (purple) together form the quasi 2D “pancake” trap. Finally, the DMD beam (yellow) is used to probe the dispersion relation of the formed BEC.

5 Outlook and Timeline

Moving forward there are several (more or less distinct and sometimes parallel) threads which are detailed below. My involvement in each of these tasks will vary with the initial focus on completion of science cell and magnetic field setups.

Erbium BEC experiments in the MOT chamber

There are several important experiments to be carried out on our Erbium BEC in the MOT chamber:

- We are currently undertaking a detailed study of the three-body loss coefficient in 166Er which will be important for future experiments; see Section 6.3.1 for current progress. The data taking for this will be completed in September 2022 and the work written up to be submitted for publication by December 2022.
- By utilizing the tunability of our (two beam) optical dipole trap we will explore how the BEC/droplet/supersolid phase diagram depends on the trap aspect ratio. Data taking in September and October 2022 followed by analysis and publication.

Transport of Er atoms to science cell

We are currently designing a feedback system to stabilise our tuneable lenses, this is expected to be finished by the end of September 2022. At this point transport of the erbium atoms

Completion of Science cell magnetic-field and optical setups

This will be my main focus in the next few months and will proceed as follows:

- Finalise design of coils (October 2022).
- Complete design of science cell optical setup (November - December 2022).
- Install coils (February 2023).
- Install optical setup (March 2023).
- Create optical pancake box trap and trap Erbium/Potassium atoms (April - May 2023).

Erbium experiments in pancake box trap

- These will begin by characterising the dispersion relation (and how it depends on the relative strength of contact and dipolar interactions) using Bragg spectroscopy (June 2023 onwards).
- Experiments on supersolid and droplet structures in box potential (August 2023 onwards).
- Non-equilibrium studies of quenched and driven systems (August 2023 onwards)

Add potassium 2D-MOT and create and characterise Er-K mixture

The addition of potassium atoms to our experiment is key for some future scientific objectives (see below). Both the additional vacuum and optics setups for the implementation of a potassium 2D-MOT to our existing vacuum system are largely ready and so will proceed as follows:

- Add K 2D+ MOT vacuum extension and perform bake-out (November 2022).
- Achieve and optimise K 2D+ MOT (December 2022 - January 2023).
- Obtain and Optimise K 3D MOT (February - March 2023).
- Characterize Er, K and inter species Feshbach resonances, optimize dual species evaporation, transport and trapping (April - July 2023).

K in Er impurity experiments in pancake box trap

The two main directions that will be pursued initially are:

- Measurements of the energy and effective mass of the dipolar polaron formed by having a K impurity in a dipolar reservoir (August - December 2023).
- Explore the possible Non-Markovian behaviour of an impurity qubit interacting with a dipolar reservoir (January - June 2024).

6 Appendix

6.1 Inductance Code verification

The mutual inductance code was tested against an approximation of the mutual inductance. This approximation is effective when the coil generating the fields (coil 1) radius is much greater than the radius of the coil the field is applied to (coil 2) (R1>>R2).
We can calculate the field generated by coil 1 on the centre of coil 2 using (9)

$$B = \frac{\mu_0 I_1 R_1^2}{2(R_1^2 + x^2)^{3/2}} \tag{9}$$

As $R_1 >> R_2$ we can say that the field is acting on the full loop area hence

$$\phi = B \times A_2 = \frac{\mu_0 I_1 R_1^2}{2(R_1^2 + x^2)^{3/2}} \times \pi R_2^2 \tag{10}$$

then using equation 5 the mutual inductance can be approximated to equation (11) for the case of $R_1 >> R_2$

$$M = \frac{\mu_0 \pi R_1^2 R_2^2}{2(R_1^2 + x^2)^{3/2}} \tag{11}$$

This approximation allowed for a verification of the numerical solution. Results of this are shown in figure 24. In figure 24 A, R_2 and x are both kept constant at 1 (arb units) and the number of sample points set to 100. The radius of R_1 is increased to enable the condition for the approximation to be satisfied. It can then be seen that at large R_1 (i.e. $R_1 >> R_2$) the two solutions converge with approximately 7% error.
This error is explained in figure 24 B in which, R_1 and R_2 are now both fixed at 100 and 1 with x = 1 (arb units). The number of sampling points are now varied which shows that on average, an increased number of points leads to less error. However, also shown in figure 24 is a quantisation issue. This effect related to how the area points are sampled as in figure 18 B. In order for the total number of sample points to approximately equal N it was decided that there would be $\lfloor\sqrt{N}/3\rfloor$ rings and $\lfloor\sqrt{N}\rfloor$ points per ring. This implies that whenever N increases past a square number, the number of points in each ring increases by 1. However, the more significant error source is occurs when the square root of N is also divisible by 3 in which case the number of rings increases by 1. Both of these lead to a change in how the point sample is distributed and therefore the accuracy of the simulation is affected around these N values. This code was only designed for an order of magnitude calculation and therefore, it was determined that this error was acceptable. However, if more accuracy was required then the sampling method would require to be improved.

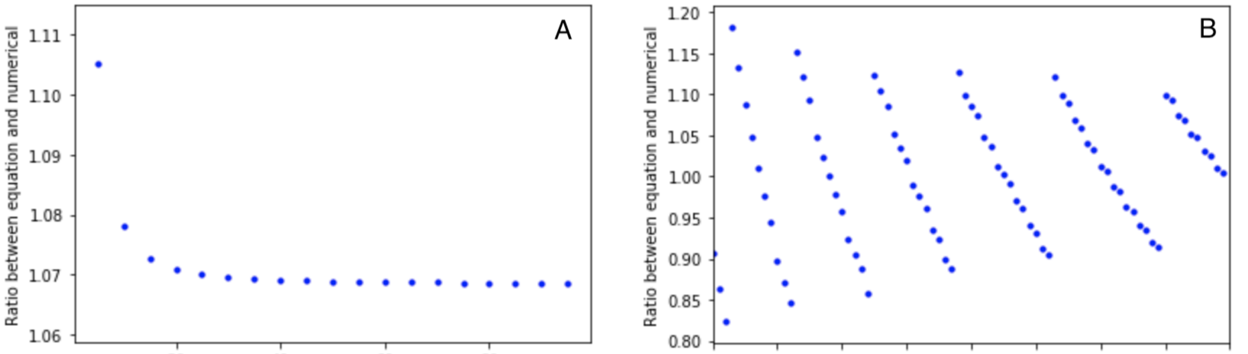

Figure 24: The ratio between the numerical solution and analytical approximation (for r1 >> r2). A shows how the error decreases as the radius of one coil (r1) is increased such that the approximation is more closely followed, however, the trend is to ≈7% error for 250 sampling points. In B r1 is kept constant at 100 and the number of points are varied. The trend is that at higher point number average error decreases however it also shows two separated quantisation issues due to the sampling technique. This could be improved with better sampling however for the purpose required this solution was adequate.

6.2 Making the RF coils

The MOT chamber is a large stainless steel shell with small glass viewing windows. If the coils are placed far outside this chamber, the AC field will produce eddy currents in the chamber walls which will act to cancel the field produced. It was therefore chosen to make a set of coils which could be placed at the edge of the viewpoint to minimise this effect. These coils are shown pictured in situ in figure 25. The coils were hand wound around a template with various wire thicknesses and turn numbers. These were then tested by first applying a AC signal to a 'driving coil' and then using a second 'pick up' coil to measure the field at same the distance between the view port and centre of the MOT chamber. An example of this can be seen in figure 26. This testing was made difficult due to nearby metal objects interfering with the AC field. It was therefore decided to attempt to observe cloud splitting with the 30 turn coil and then a 40 turn coil. These coils were constructed of 0.5mm wire and would be driven at ≈ 4 MHz 0.5 Vpp through an amplifier with 24dB of gain [38]. We would expect there to be around 0.03 G produced by this setup. An important consideration is that continuing to increase the turn number will not necessarily lead to a higher field strength as the self inductance of the coil will increase.

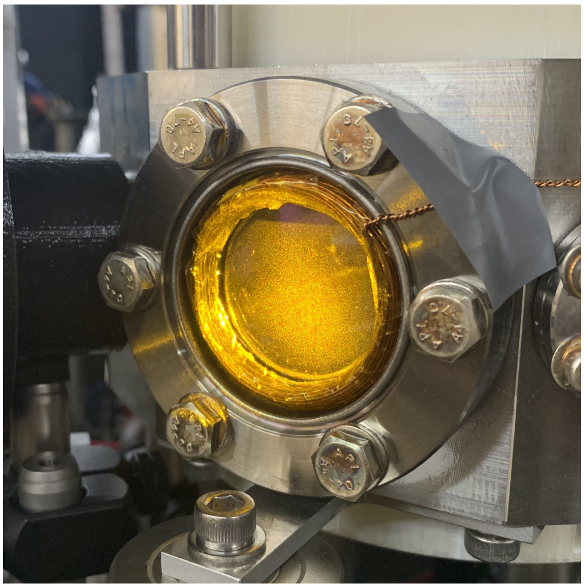

Figure 25: RF coil (annealed copper wire) in position in the edge of a view port.

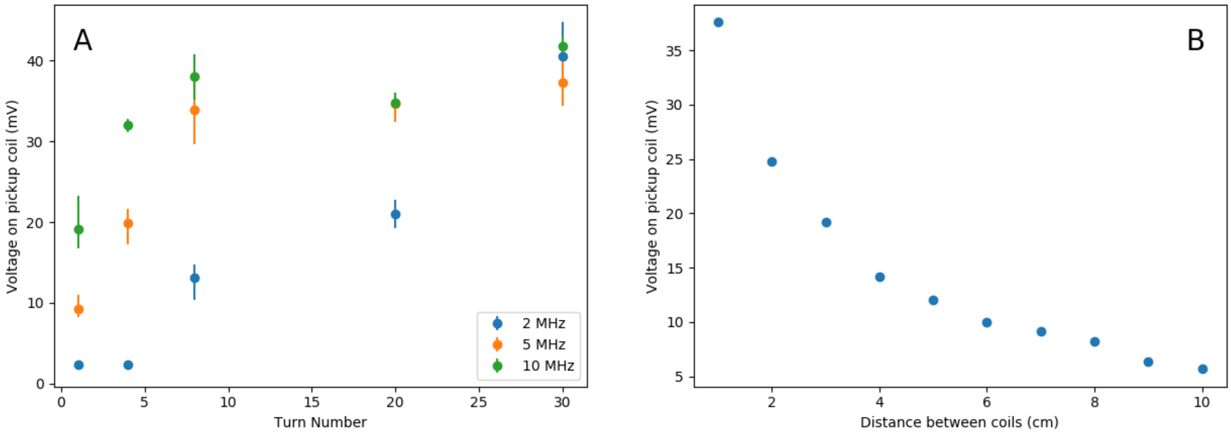

Figure 26: Tests of the RF coil. A shows how the voltage pickup on a second coil decreases with distance to the 11cm point (distance between view port and centre of MOT chamber). B shows how the pick up coil voltage depends on both frequency of applied voltage and turn number. This data is quite noisey due to metal objects interfering with the AC field. It was therefore chosen to atempt to see cloud splitting with a 30 and 40 turn coil

6.3 Addition Work completed in the group

6.3.1 Three Body Loss

A three body event is a process in which a 2 atom compound interacts with a third atom. This can contribute to significant losses within an ultra cold atom experiment and therefore understanding it is vital. Three body loss is density dependant and therefore occurs at the centre of the trap containing the densest but also coldest atoms. This loss therefore can be thought of an anti-evaporation in that there is a selectivity to lose the coldest atoms such that upon rethermalisation the temperature of the atomic gas increases. The three body loss coefficient, L_3 is proportional to the scattering length, a_s to the forth power.

$$L_3 = \frac{n_l C}{m} a_s^4 \tag{12}$$

Here n_l is the number of atoms lost in a recombination event, C is a dimensionless parameter which ranges from 0 to 70 and m is the mass of the atom. The dynamics of the system can be quantitatively explained by two coupled non linear differential equations for the number (N) and temperature (T) of the atoms, equations 13 and 14 [39].

$$\frac{dN}{dt} = -\alpha N - \gamma \frac{N^3}{T^3} \tag{13}$$

$$\frac{dT}{dt} = \gamma \frac{N^2}{T^3} \frac{(T + T_h}{3} \tag{14}$$

Here α, γ and T_h are the fitting parameters with $\gamma = L_3(m\omega^2/2\pi k_B)^3/\sqrt{27}$ An example of a fit is shown in figure 27.

Three body lose is closely related to Feshbach resonances as both involve the coupling of free and bound states. Therefore if the 3 body loss coefficient, γ is plotted against magnetic field then Feshbach resonances will be seen as peaks in γ. Data is taken across a range of field and results shown in figure 28. The data taking as well as fitting work was completed by a fellow DPhil student, Peter Juhasz.

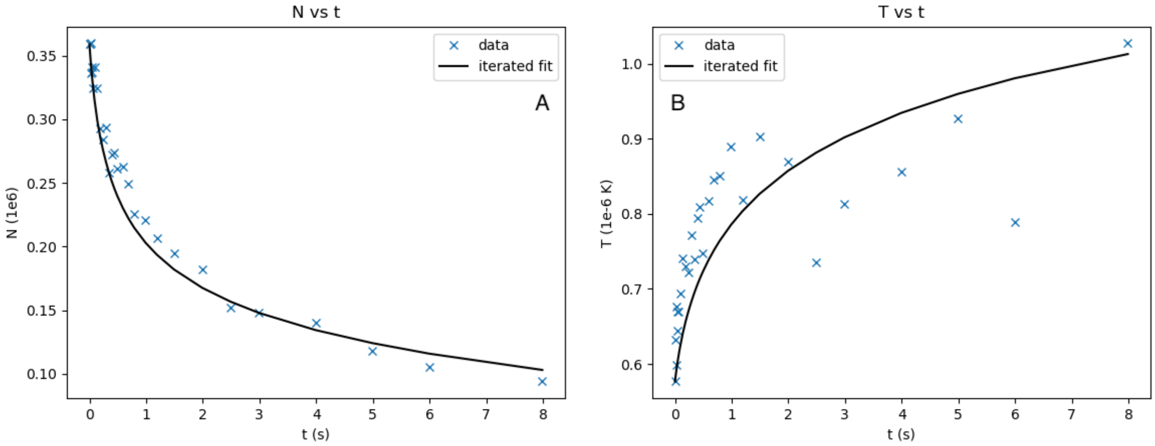

Figure 27: Fits of both number (N) and temperature (T) against time. The fit parameters can be used to extract the 3 body loss coefficient, γ

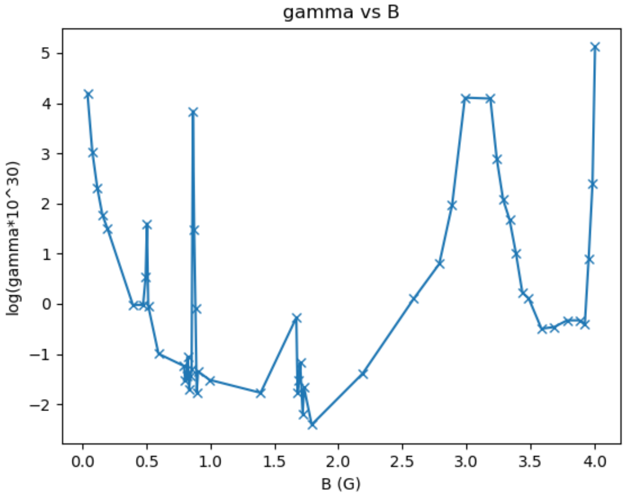

Figure 28: Three body lose parameter γ against magnetic field. Peaks show the positions of Feshbach resonances.

6.3.2 BEC Machine Learning Fit

During the evaporative cooling ramp, the phase space density increases such that the finite number of excited states are filled. The remaining atoms in the cloud then begin to fill the lowest energy state thereby forming a BEC. At this point, the cloud is not purely a quantum gas or thermal cloud, but can rather be represented by a bimodal distribution. The thermal cloud can be modelled with the enhanced Bose distribution, whereas the BEC is modelled with the Thomas-Fermi approximation thereby yielding a three dimensional parabolic distribution.

During the experimental cycle, an absorption image is taken of the cloud, as shown in figure 29A, which essentially integrates the atomic density distribution along one axis. The integrated enhanced Bose distribution n_{th} can be represented by,

$$n_{th}(x,y) = n_{0th} g_2 \left[e^{\beta} e^{-\frac{1}{2}\left(\frac{x^2}{\sigma_x^2}+\frac{y^2}{\sigma_y^2}\right)} \right] \tag{15}$$

where n_{0th} is the peak atomic density, g_2 is the polylog function and σ_x and σ_y are the thermal cloud widths. Furthermore, $\beta = \frac{\mu}{k_b T}$ where μ is the chemical potential and T is the temperature, but during analysis we generally assume $\beta = 1$. Next, the integrated BEC density $n_{bec}(x,y)$ is given by,

$$n_{bec}(x,y) = n_{0bec} \left(1 - \frac{x^2}{R_x^2} - \frac{y^2}{R_y^2} \right)^{\frac{3}{2}} \tag{16}$$

where n_{0bec} is the peak atomic density and R_x and R_y are the widths of the BEC cloud. Finally, the total integrated density is given by,

$$n_{tot}(x,y) = n_{th}(x,y) + n_{bec}(x,y) \tag{17}$$

Determining the number of atoms in the thermal cloud and BEC as well as calculating the condensate fraction requires extracting the various parameters in equation 15 and 16. We do this with the following complex fitting procedure. First, the image is summed along both the x and y axes as shown in figure 29(B-C) and the data along each axis is fit its own 1D Gaussian. These fits are then used to seed a bimodal 1D fit on each set of summed 1D data where the bimodal fit is composed of a 1D Gaussian, which is a good approximation for the enhanced Bose distribution, and a 1D parabola for the BEC.

These 1D bimodal fits are then converted to 2D seeds such that a bimodal 2D fit can be done on the image data. This bimodal fit is composed of 2D Gaussian and a 2D parabola for the thermal and BEC portions of the cloud respectively. The 2D fit parameters for the BEC are then used to construct an elliptical data mask which masks out image data containing the BEC. Since the remaining data is comprised solely of the thermal cloud, this is fit with equation 15 to accurately determine the thermal cloud parameters as shown in figure 29E. Using the extracted thermal cloud parameters, the atomic density due to the thermal cloud is calculated and then subtracted from the original image leaving only the BEC atomic density. Finally, this remaining data is fit with equation 16 to determine the BEC parameters as shown in figure 29F. With both the thermal cloud parameters and BEC cloud parameters, the bimodal distribution can be completely reconstructed as shown in 29D. This work was completed by fellow DPhil student Lucas Hofer.

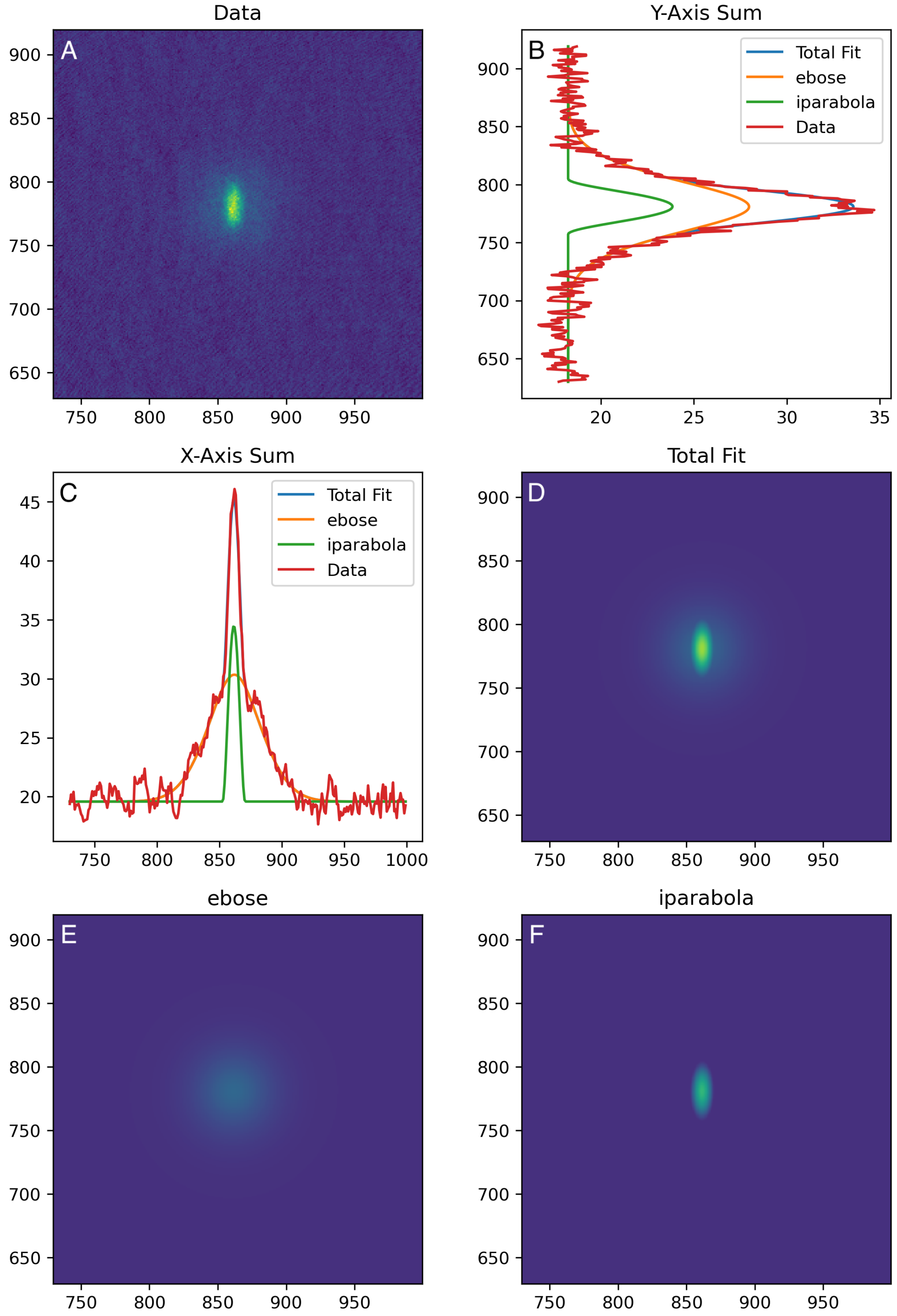

Figure 29: Plots showing fitting of the atomic distribution which contains both a BEC (parabola) and thermal cloud (extended Bose distribution). A shows the raw data taken by an absorption image. B and C show pixel sums across both orthogonal directions with total fit, extended Bose distribution, BEC parabola and raw data shown. D, E and F show the individual 2D fits which can be used to extract the number of each component of the atomic cloud.

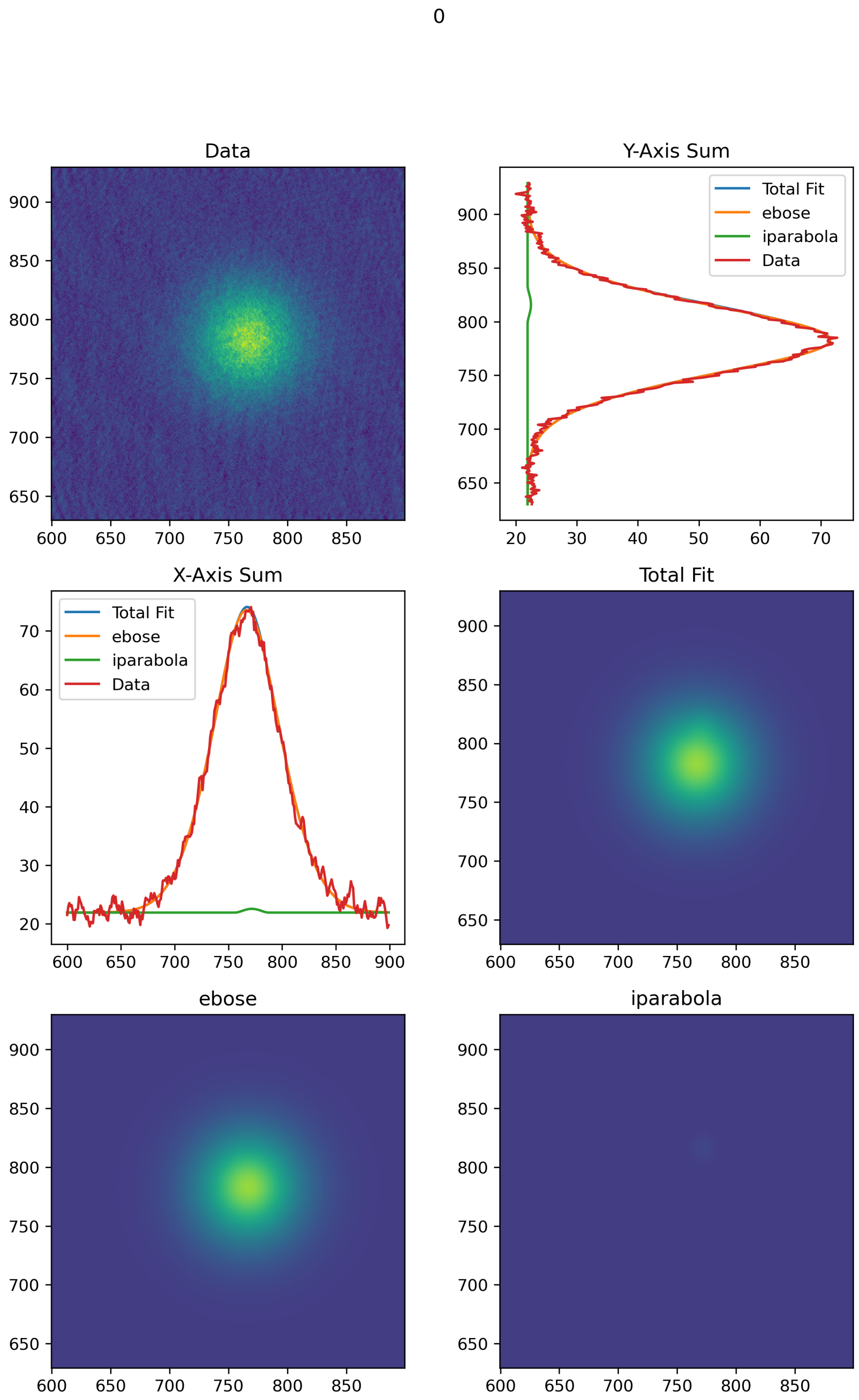

Figure 30: Fitting of the thermal cloud shown as left graph in figure 7.

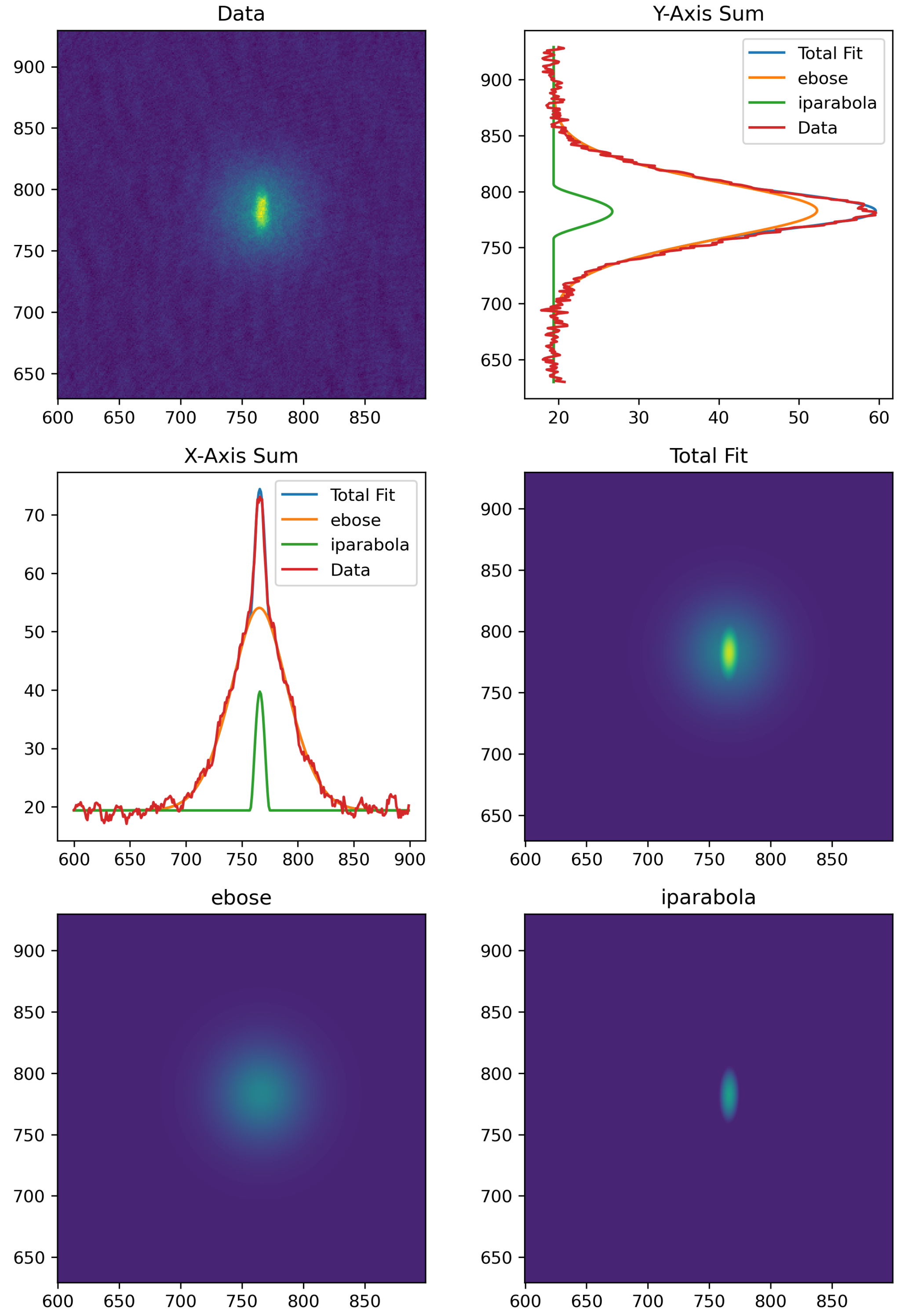

Figure 31: Fitting of the thermal cloud BEC mixture shown as middle graph in figure 7

9

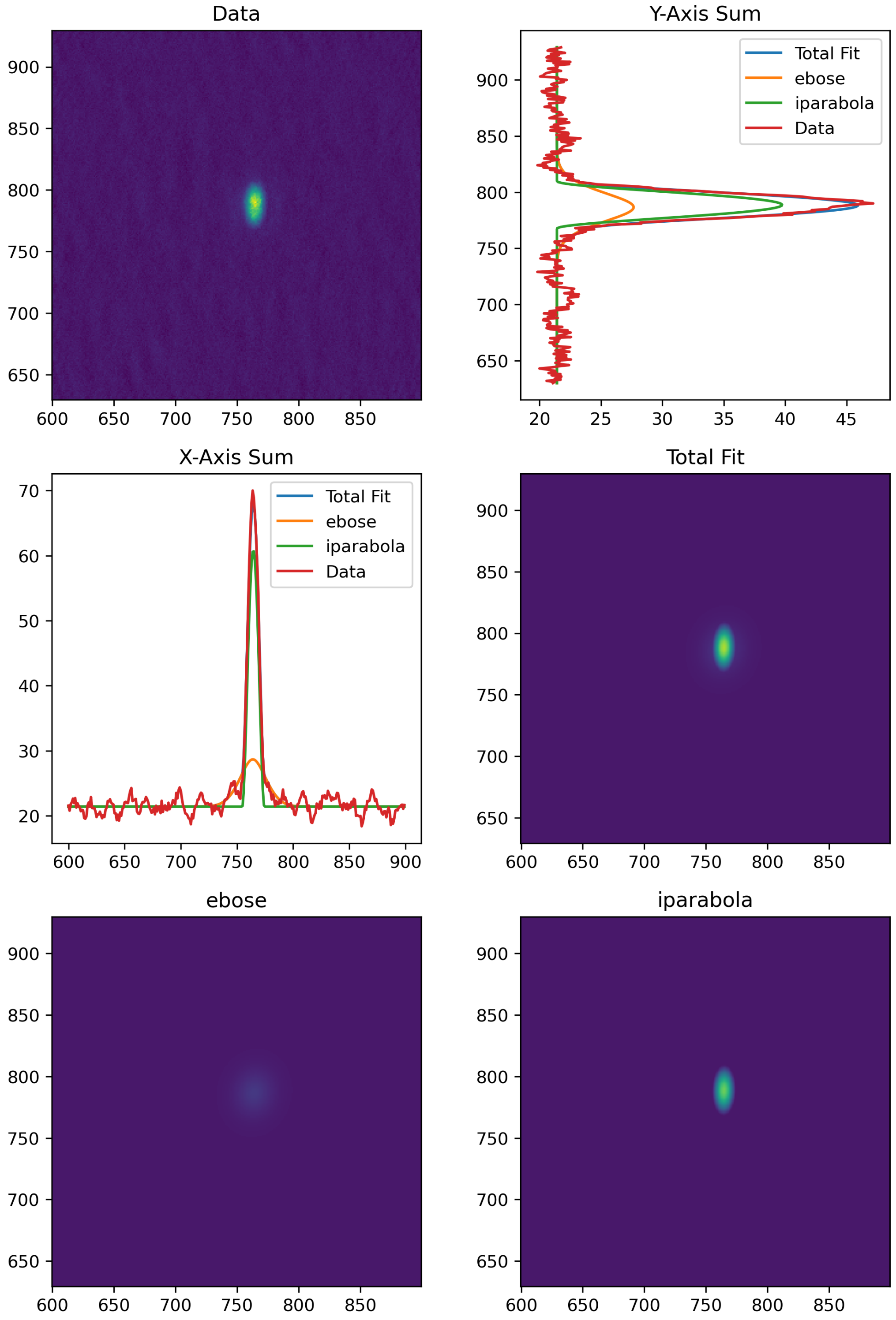

Figure 32: Fitting of the BEC shown as right graph in figure 7

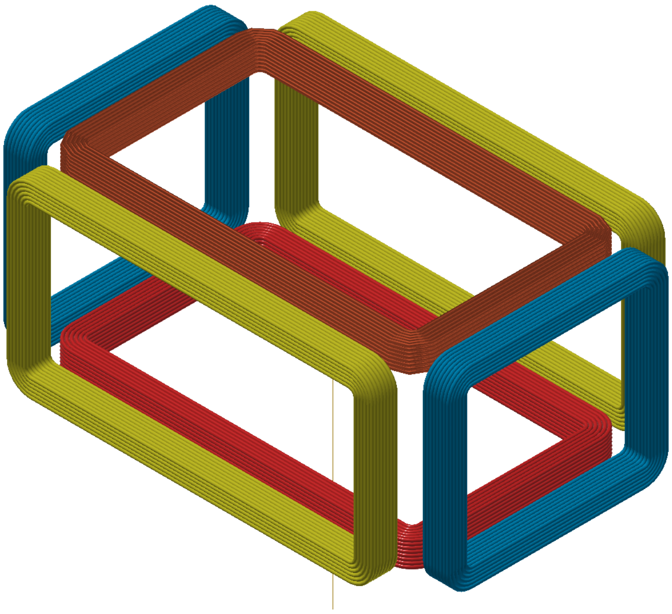

Figure 33: The original coil design. The X,Y and Z coils are shown in Yellow, Blue and Red respectively.

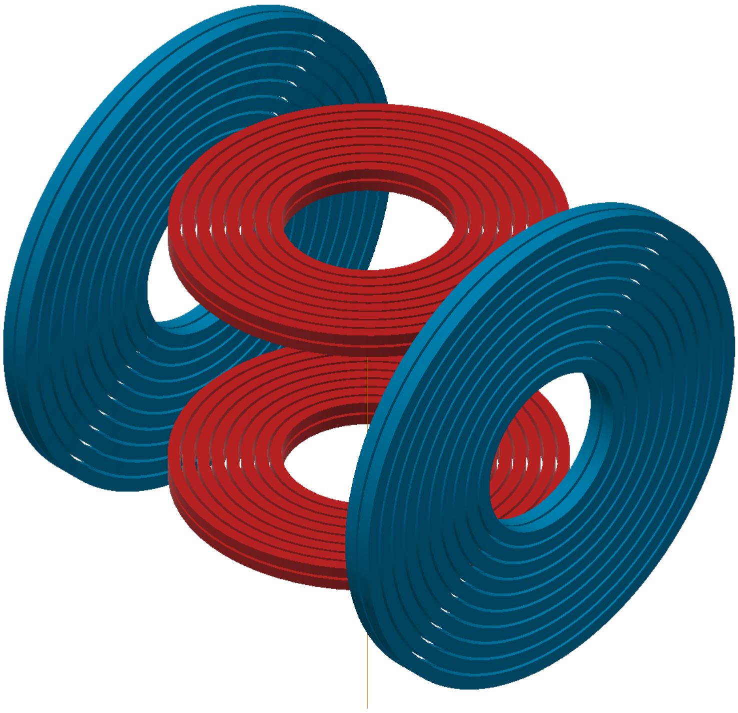

Figure 34: The original coil design. The Y and Z coils are shown in Blue and Red respectively.

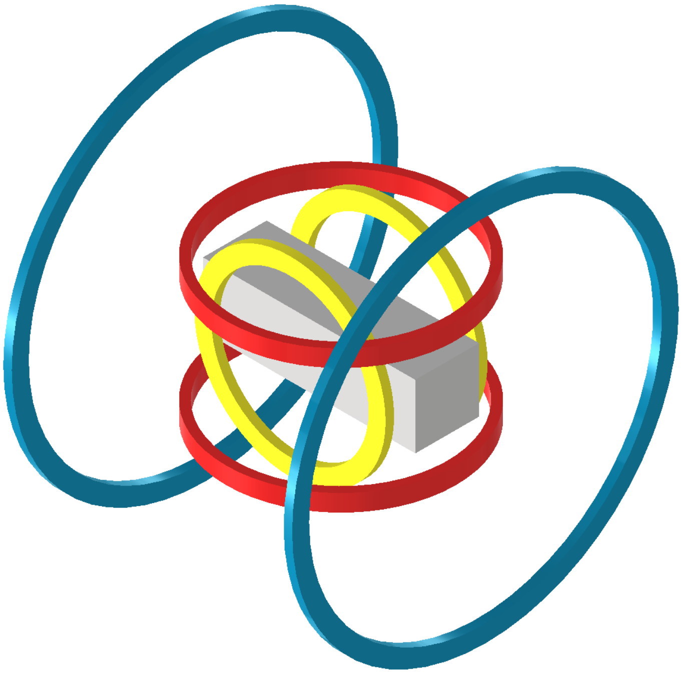

Figure 35: The updated and optimised fast coil design. The X,Y and Z coils are shown in Yellow, Blue and Red respectively.

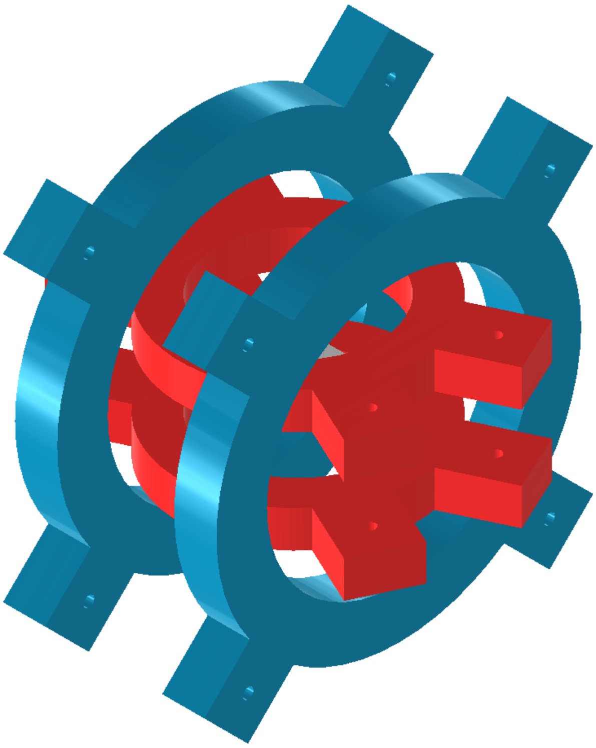

Figure 36: The updated and optimised large coil design. The Y and Z coils are shown in Blue and Red respectively.

References

[1] Anderson, M.H., Ensher, J.R., Matthews, M.R., Wieman, C.E. and Cornell, E.A., 1995. Observation of Bose-Einstein condensation in a dilute atomic vapor. science, 269(5221), pp.198-201.

[2] Davis, K.B., Mewes, M.O., Andrews, M.R., van Druten, N.J., Durfee, D.S., Kurn, D.M. and Ketterle, W., 1995. Bose-Einstein condensation in a gas of sodium atoms. Physical review letters, 75(22), p.3969.

[3] (2001) 'The Nobel Prize in Physics 2001', Available at: https://www.nobelprize.org/prizes/physics/2001/summary/ (Accessed: 04/07/22)

[4] Aikawa, K., Frisch, A., Mark, M., Baier, S., Rietzler, A., Grimm, R. and Ferlaino, F., 2012. Bose-Einstein condensation of erbium. Physical review letters, 108(21), p.210401.

[5] Modugno, G., Ferrari, G., Roati, G., Brecha, R.J., Simoni, A. and Inguscio, M., 2001. Bose-Einstein condensation of potassium atoms by sympathetic cooling. Science, 294(5545), pp.1320-1322.

[6] NIST/JILA/CU-Boulder

[7] Griesmaier, A., Werner, J., Hensler, S., Stuhler, J. and Pfau, T., 2005. Bose-Einstein condensation of chromium. Physical Review Letters, 94(16), p.160401.

[8] Lu, M., Burdick, N.Q., Youn, S.H. and Lev, B.L., 2011. Strongly dipolar Bose-Einstein condensate of dysprosium. Physical review letters, 107(19), p.190401.

[9] Feynman, R.P. and Cohen, M., 1956. Energy spectrum of the excitations in liquid helium. Physical Review, 102(5), p.1189.

[10] Santos, L., Shlyapnikov, G.V. and Lewenstein, M., 2003. Roton-maxon spectrum and stability of trapped dipolar Bose-Einstein condensates. Physical review letters, 90(25), p.250403.

[11] Kadau, H., Schmitt, M., Wenzel, M., Wink, C., Maier, T., Ferrier-Barbut, I. and Pfau, T., 2016. Observing the Rosensweig instability of a quantum ferrofluid. Nature, 530(7589), pp.194-197.

[12] Ferrier-Barbut, I., Kadau, H., Schmitt, M., Wenzel, M. and Pfau, T., 2016. Observation of quantum droplets in a strongly dipolar Bose gas. Physical review letters, 116(21), p.215301.

[13] Bisset, R.N., Wilson, R.M., Baillie, D. and Blakie, P.B., 2016. Ground-state phase diagram of a dipolar condensate with quantum fluctuations. Physical Review A, 94(3), p.033619.

[14] Chomaz, L., Baier, S., Petter, D., Mark, M.J., Wächtler, F., Santos, L. and Ferlaino, F., 2016. Quantum-fluctuation-driven crossover from a dilute Bose-Einstein condensate to a macrodroplet in a dipolar quantum fluid. Physical Review X, 6(4), p.041039.

[15] Astrakharchik, G.E., Boronat, J., Kurbakov, I.L. and Lozovik, Y.E., 2007. Quantum phase transition in a two-dimensional system of dipoles. Physical review letters, 98(6), p.060405.

[16] Léonard, J., Morales, A., Zupancic, P., Esslinger, T. and Donner, T., 2017. Supersolid formation in a quantum gas breaking a continuous translational symmetry. Nature, 543(7643), pp.87-90.

[17] Li, J.R., Lee, J., Huang, W., Burchesky, S., Shteynas, B., Top, F.Ç., Jamison, A.O. and Ketterle, W., 2017. A stripe phase with supersolid properties in spin–orbit-coupled Bose–Einstein condensates. Nature, 543(7643), pp.91-94.

[18] Myatt, C.J., Burt, E.A., Ghrist, R.W., Cornell, E.A. and Wieman, C.E., 1997. Production of two overlapping Bose-Einstein condensates by sympathetic cooling. Physical Review Letters, 78(4), p.586.

[19] Hewson, A.C., 1997. The Kondo problem to heavy fermions (No. 2). Cambridge university press.

[20] Lanzara, A., Bogdanov, P.V., Zhou, X.J., Kellar, S.A., Feng, D.L., Lu, E.D., Yoshida, T., Eisaki, H., Fujimori, A., Kishio, K. and Shimoyama, J.I., 2001. Evidence for ubiquitous strong electron–phonon coupling in high-temperature superconductors. Nature, 412(6846), pp.510-514.

[21] Mannella, N., Yang, W.L., Zhou, X.J., Zheng, H., Mitchell, J.F., Zaanen, J., Devereaux, T.P., Nagaosa, N., Hussain, Z. and Shen, Z.X., 2005. Nodal quasiparticle in pseudogapped colossal magnetoresistive manganites. Nature, 438(7067), pp.474-478.

[22] L. D. Landau, Electron motion in crystal lattices, Phys. Z. Sowjetunion 3, 664 (1933)

[23] Raab, E. L., Prentiss, M., Cable, A., Chu, S., Pritchard, D. E. (1987). Trapping of neutral sodium atoms with radiation pressure. Physical review letters, 59(23), 2631.

[24] Phillips, W. D., Metcalf, H. (1982). Laser deceleration of an atomic beam. Physical Review Letters, 48(9), 596.

[25] (2022) 'The Nobel Prize in Physics 1997', https://www.nobelprize.org/prizes/physics/1997/press-release/ (Accessed: 04/07/22)

[26] Chomaz, L., van Bijnen, R.M., Petter, D., Faraoni, G., Baier, S., Becher, J.H., Mark, M.J., Waechtler, F., Santos, L. and Ferlaino, F., 2018. Observation of roton mode population in a dipolar quantum gas. Nature physics, 14(5), pp.442-446.

[27] Foot, Christopher J. Atomic physics. Vol. 7. OUP Oxford, 2004.

[28] Krstajic, M 2021, 'Experimental Platform for a Box-Trapped Dipolar Quantum Gas', PhD thesis, Cambridge University, Oxford

[29] Chin, C., Grimm, R., Julienne, P. and Tiesinga, E., 2010. Feshbach resonances in ultracold gases. Reviews of Modern Physics, 82(2), p.1225.

[30] Frisch, A 2014, 'Dipolar Quantum Gases of Erbium', PhD thesis, University of Innsbruck, Innsbruck

[31] Patscheider, A., Chomaz, L., Natale, G., Petter, D., Mark, M.J., Baier, S., Yang, B., Wang, R.R.W., Bohn, J.L. and Ferlaino, F., 2021. Accurate determination of the scattering length of erbium atoms. arXiv preprint arXiv:2112.11883.

[32] Chen, H.Z., Yao, X.C., Wu, Y.P., Liu, X.P., Wang, X.Q., Wang, Y.X., Chen, Y.A. and Pan, J.W., 2016. Production of large K 41 Bose-Einstein condensates using D 1 gray molasses. Physical Review A, 94(3), p.033408.

[33] Kishimoto, T., Kobayashi, J., Noda, K., Aikawa, K., Ueda, M. and Inouye, S., 2009. Direct evaporative cooling of K 41 into a Bose-Einstein condensate. Physical Review A, 79(3), p.031602.

[34] Private communication, C. Eigen

[35] (2022) 'Hollow Conductors', Available at: https://www.luvata.com/products/hollow-conductors (Accessed: 04/07/22)

[36] (2022) 'Magnetic Field Technology', Available at: https://www.oswald.de/en/magnetic-field-technology/ (Accessed: 04/07/22)

[37] (2022) 'High Power 1064 nm Fiber Lasers Amplifers', https://azurlight-systems.com/portfoliopage/1064-nm-high-power-fiber-lasers-amplifiers-50w-single-mode-single-frequency/ (Accessed: 04/07/22)

[38] (2022) 'ZHL-3A+', Available at: https://www.minicircuits.com/pdfs/ZHL-3A.pdf (Accessed: 04/07/22)

[39] Weber, T., Herbig, J., Mark, M., Nägerl, H. C., Grimm, R. (2003). Three-body recombination at large scattering lengths in an ultracold atomic gas. Physical review letters, 91(12), 123201.